

Hundness in twisted bilayer graphene: correlated gaps and pairing

Seongyeon Youn,^{1,2,*} Beomjoon Goh,^{1,2,3,*} Geng-Dong Zhou,⁴ Zhi-Da Song,^{4,5,6,†} and Seung-Sup B. Lee^{1,2,3,‡}

¹*Department of Physics and Astronomy, Seoul National University, Seoul 08826, Korea*

²*Center for Theoretical Physics, Seoul National University, Seoul 08826, Korea*

³*Institute for Data Innovation in Science, Seoul National University, Seoul 08826, Korea*

⁴*International Center for Quantum Materials, School of Physics, Peking University, Beijing 100871, China*

⁵*Hefei National Laboratory, Hefei 230088, China*

⁶*Collaborative Innovation Center of Quantum Matter, Beijing 100871, China*

(Dated: December 5, 2024)

We characterize gap-opening mechanisms in the topological heavy fermion (THF) model of magic-angle twisted bilayer graphene (MATBG), with and without electron-phonon coupling, using dynamical mean-field theory (DMFT) with the numerical renormalization group (NRG) impurity solver. In the presence of symmetry breaking associated with valley-orbital ordering (time-reversal-symmetric or Kramers intervalley coherent, or valley polarized), spin anti-Hund and orbital-angular-momentum Hund couplings, induced by the dynamical Jahn–Teller effect, result in a robust pseudogap at filling $2 \lesssim |\nu| \lesssim 2.5$. We also find that Hundness enhances the pairing susceptibilities for $1.6 \lesssim |\nu| \lesssim 2.8$, which might be a precursor to the superconducting phases neighboring $|\nu| = 2$.

DOI:

Introduction.—Magic-angle twisted bilayer graphene (MATBG) [1] hosts an interplay of band topology [2–7], strong electronic correlations [8–19], and electron-phonon coupling (EPC) [20–31]. Many experiments observed correlated insulators at filling $\nu = \pm 2$ per moiré unit cell (MUC) with respect to the charge neutrality point (CNP) [32–44] and unconventional superconductivity near them [37–41, 44–46]. Meanwhile, the insulating behavior is weaker or invisible at $|\nu| = 1, 3$ [32–41]. Scanning tunneling microscopy (STM) studies of the insulator at $|\nu| = 2$ revealed a pseudogap [40–42] accompanied by side peaks at its edges [40] and observed a time-reversal-symmetric intervalley coherent (TIVC) order [41] in ultralow-strain samples, which is not energetically favored over others, such as valley polarized (VP) or Kramers intervalley coherent (KIVC) orders, without considering EPC [27–29, 47–53].

Recent dynamical mean-field theory (DMFT) calculations [15–18] elucidated key features of MATBG by capturing strong correlations: the formation and screening of local moments, cascade transitions, and their temperature dependence, to name a few. However, they found a gap at $|\nu| = 1$ that is more significant than $|\nu| = 2$, which implies extra ingredients are necessary. Also, it has been unclear how Mott-like features [32, 43] arise on top of the observed TIVC order, given that symmetry breaking often competes with dynamical correlations.

In this Letter, we demonstrate that the interplay between EPC-induced (anti-)Hund couplings and valley-orbital ordering is responsible for opening a pseudogap with side peaks, over an extended region of $2 \lesssim |\nu| \lesssim 2.5$. We incorporate the latter by downfolding the topological heavy fermion (THF) model [15–17, 54–64] of MATBG, imposing a valley-orbital order. By solving the downfolded model using DMFT [65] with the numerical renormalization group (NRG) [66–72] impurity solver, we reveal that

the effective Hund couplings invoke the Janus effect [73–77] that favors gap opening at the half filling of the active interacting orbitals, corresponding to the range of $|\nu|$. Hundness also facilitate fluctuations of electron pairs with a specific symmetry, over a range of ν overlapping with the reported superconducting domes [39–41, 44–46].

Valley-orbital-ordered THF model.—The THF model [54, 55] consists of two interacting f orbitals ($\alpha = 1, 2$) localized at the AA-stacking region of each MUC, hybridized with four topological Dirac c bands, per spin ($\sigma = \uparrow, \downarrow$) and valley ($\eta = \pm$). At CNP ($\nu = 0$), the Kondo screening of f electrons is suppressed since the density of states for the c bands vanishes at the Fermi level. Thus f electrons are susceptible to valley-orbital ordering via Ruderman–Kittel–Kasuya–Yosida (RKKY) interactions [13, 17, 51, 54, 78]. When doped to $\nu > 0$, excess electrons experience Kondo correlations due to finite hybridization. To incorporate both effects, we first downfold the THF model onto the active subspace of excess electrons, on top of the valley-orbital order at CNP chosen among the VP, KIVC, and TIVC states.

The downfolded, valley-orbital-ordered THF (VTHF) model for $\nu > 0$ [17, 79] has two f valley-orbitals per MUC and four c bands per spin. (For brevity, we call f “orbitals” also for the VTHF model, in the rest of this paper.) Its Hamiltonian is

$$H_{\text{VTHF}} = \sum_{\mathbf{R}} \frac{U_1}{2} N_{\mathbf{R}}^f (N_{\mathbf{R}}^f - 1) + \sum_{\mathbf{k} \alpha \alpha'} h_{\alpha \alpha'}^c(\mathbf{k}) c_{\mathbf{k} \alpha \sigma}^\dagger c_{\mathbf{k} \alpha' \sigma} + \sum_{\mathbf{k} \alpha l \sigma} (h_{\alpha l}^{cf}(\mathbf{k}) c_{\mathbf{k} \alpha \sigma}^\dagger f_{\mathbf{k} l \sigma} + \text{h.c.}) - \mu N + H_{\text{nonloc}}, \quad (1)$$

where $f_{\mathbf{R} l \sigma}^\dagger$ creates a spin- σ electron at the f orbital of angular momentum $l = \eta(-1)^{\alpha-1} = \pm 1 \pmod{3}$ centered at position \mathbf{R} and $f_{\mathbf{k} l \sigma}^\dagger$ is its Fourier transform. (In single-site DMFT, the C_{3z} rotation symmetry is promoted to the

$U(1)_{\text{orbital}}$ symmetry [26].) $c_{\mathbf{k}a\sigma}^\dagger$ creates a spin- σ electron with momentum \mathbf{k} in the c band of index $a = 1, 2, 3, 4$. $N_{\mathbf{R}}^f = \sum_{l\sigma} f_{\mathbf{R}l\sigma}^\dagger f_{\mathbf{R}l\sigma}$ and N count the f electrons at \mathbf{R} and all electrons, respectively, with respect to CNP.

The strength $U_1 = 57.95$ meV of the SU(4) symmetric Hubbard interaction and the parameters for the nonlocal interactions H_{nonloc} remain the same as in the original THF model [54], while the c -band dispersion h^c and the c - f hybridization h^{cf} may depend on the choice of the valley-orbital order [80]. We consider the flat band limit [17, 54] in which h^c describes massless Dirac dispersion and thus H_{VTHF} is indistinguishable between the VP and KIVC cases, putting aside different basis transformations $(\alpha, \eta) \rightarrow l$. We tune the chemical potential μ to study a range of $\nu = \langle N \rangle / n_M = \nu^f + \nu^c \in [0.8, 3.2]$ and $\nu^f = \langle \sum_{\mathbf{R}} N_{\mathbf{R}}^f \rangle / n_M$, where n_M is the number of MUCs.

Effective Hund couplings from EPC.—Similarly as in fullerenes [81–85], the dynamical Jahn–Teller effect introduces spin anti-Hund (J_S) and orbital-angular-momentum Hund (J_L) couplings [24–28] to the VTHF model,

$$H_{\text{EPC}} = \sum_{\mathbf{R}} [2J_S \mathbf{S}_{\mathbf{R},+1} \cdot \mathbf{S}_{\mathbf{R},-1} - J_L (L_{\mathbf{R}}^2 - N_{\mathbf{R}}^f) + \tilde{U} N_{\mathbf{R}}^f (N_{\mathbf{R}}^f - 1)/2], \quad (2)$$

where $\mathbf{S}_{\mathbf{R}l}$ is the f -electron spin operator for orbital l at \mathbf{R} and $L_{\mathbf{R}} = \sum_{l\sigma} l f_{\mathbf{R}l\sigma}^\dagger f_{\mathbf{R}l\sigma}$ measures f -electron orbital angular momentum at \mathbf{R} [26, 28]. The parameters of H_{EPC} depend on the order: $(J_S, J_L, \tilde{U}) = (0.610, 0.069, 0.648), (0.062, 0.605, 0.511), (0.672, 0.084, -0.530)$ meV for the VP, KIVC, and TIVC orders, respectively [80].

To study phases at $\nu > 0$, we obtain symmetric (i.e., paramagnetic) normal-state solutions of H_{VTHF} , with and without H_{EPC} , for the VP, KIVC, and TIVC orders, by treating the correlations from Hubbard U_1 and H_{EPC} dynamically with DMFT+NRG and those from H_{nonloc} statically with Hartree mean-field approximation [17, 79, 80]. Since H_{VTHF} is identical and H_{EPC} differs between VP and KIVC, there are five distinct scenarios. The results for $\nu < 0$ are obtained by particle-hole transformation [17, 54, 86] $(\nu, \omega) \leftrightarrow (-\nu, -\omega)$, where ω is frequency.

Gap classification.—We explain how we classify the f -electron spectral gap. Within the DMFT description of a heavy-fermion type model (including the THF and VTHF models), the local f -electron Green's function is given by $G^f(\omega) = [\omega + \mu - \Sigma(\omega) - \Delta(\omega)]^{-1}$, where $\Sigma(\omega) = \Sigma'(\omega) + i\Sigma''(\omega)$ is the self-energy including the static Hartree energy from nonlocal interactions, and $\Delta(\omega) = \Delta'(\omega) + i\Delta''(\omega)$ is the hybridization function between the f orbital and the rest of the system. Here we omit l, σ indices since we focus on symmetric solutions.

The local f -electron spectral function,

$$A^f(\omega) = \frac{-\frac{1}{\pi}(\Sigma''(\omega) + \Delta''(\omega))}{(\omega + \mu - \Sigma'(\omega) - \Delta'(\omega))^2 + (\Sigma''(\omega) + \Delta''(\omega))^2}, \quad (3)$$

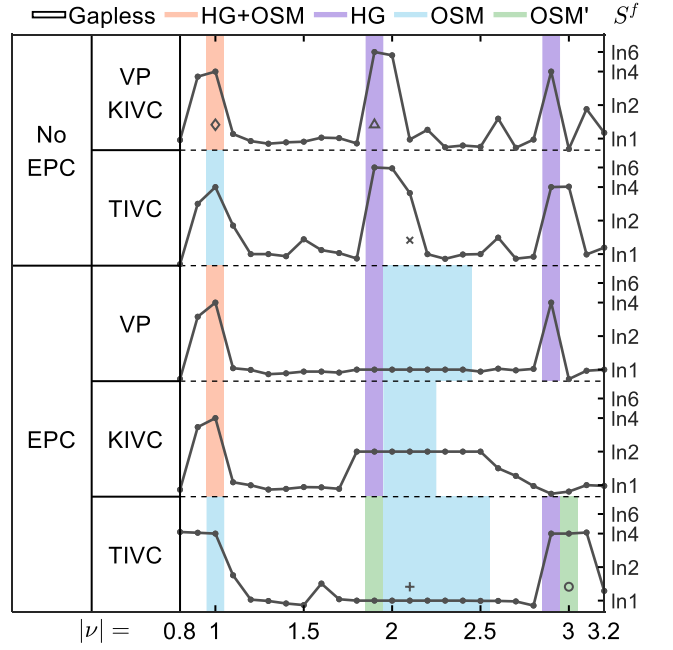


FIG. 1. Phase diagram of the VTHF model at $T = 10^{-6}$ meV as a function of filling ν , for different valley-orbital orders without and with EPC. In white regions, the spectral function is gapless. Shades indicate phases with hard gaps (HG+OSM and HG) such that $A_{\text{tot}}^f(\omega = 0) < 5 \times 10^{-4}$ /meV, $A_{\text{1MBZ}}^c(0) < 10^{-5}$ /meV and phases with pseudogaps (OSM and OSM') such that $A_{\text{tot}}^f(0) < 0.016$ /meV, $A_{\text{1MBZ}}^c(0) < 0.025$ /meV. Here $A_{\text{tot}}^f(\omega) = \sum_{l\sigma} A_{l\sigma}^f(\omega)$ and $A_{\text{1MBZ}}^c(\omega) = n_M^{-1/2} \sum_{\mathbf{k} \in \text{1MBZ}} \sum_{a\sigma} A_{a\sigma}^c(\mathbf{k}, \omega)$ are local f - and c -electron spectral functions, respectively, and 1MBZ means the first moiré Brillouin zone. Solid lines represent the f -electron contribution to the entropy per MUC, S^f , computed as the impurity entropy of the self-consistent impurity model [87] within DMFT. Spectral properties for five states specified by markers are shown in Fig. 2.

opens a gap with a small $A^f(\omega = 0)$, when the numerator is small, or the denominator is large on the RHS. (i) For the former, both $\Sigma''(0)$ and $\Delta''(0)$ must vanish. That is, $\Delta''(\omega)$ has a gap at $\omega = 0$, which we call *hybridization gap* (HG) [cf. Fig. 2 (a)]. The latter case holds when $|\Sigma(0) - \mu|$ or $|\Delta(0)|$ is large. (ii) In the *OSM* phase [88–92], a self-energy pole (Σ pole) appears as a sharp peak in $-\Sigma''(\omega)$, accompanied by (via the Kramers–Kronig relations) a pair of negative and positive peaks in $\Sigma'(\omega)$ next to it [cf. Fig. 2 (b,d)]. When the Σ pole is at or near $\omega = 0$, $|\Sigma'(0) - \mu|$ or $-\Sigma''(0)$ becomes huge, respectively, leading to a small $A^f(\omega = 0)$. (iii) We find a situation where $|\Sigma'(0) - \mu|$ is large and Σ strongly depends on ω , yet there is no self-energy pole [cf. Fig. 2 (e)]; we coin it *OSM'* based on its similarity to and difference from OSM. (iv) Lastly, a *Kondo insulator* is characterized by a pole in Δ near or at $\omega = 0$ [65, 67, 93]. We emphasize that these gap-opening mechanisms may coexist since the conditions are not exclusive, except for OSM vs OSM'.

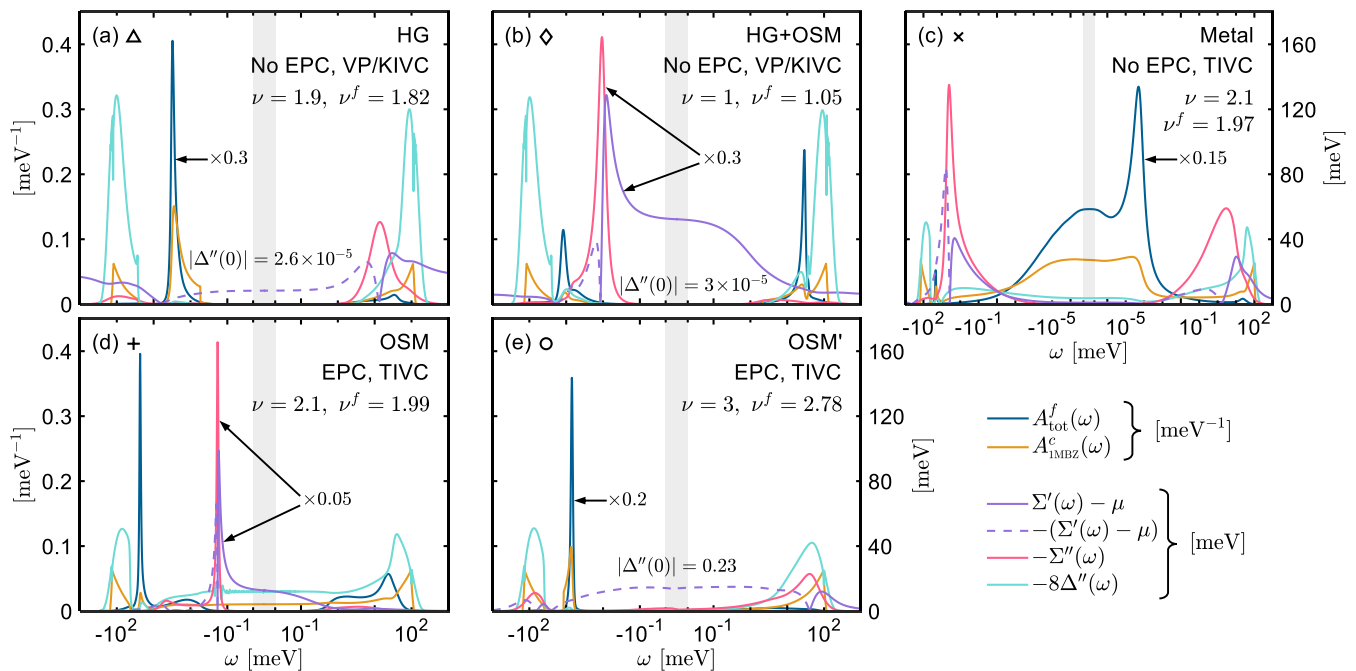


FIG. 2. Spectral properties of the VTHF model for parameters denoted by markers in the phase diagram (Fig. 1). Local spectral functions $A_{\text{tot}}^f(\omega)$ (blue) and $A_{\text{1MBZ}}^c(\omega)$ (orange) are in units of meV^{-1} (left ordinate), while the self-energy shifted by the chemical potential, $\Sigma(\omega) - \mu$ (purple for the real part, magenta for the imaginary part), and the hybridization function $\Delta(\omega)$ (cyan for the imaginary part) are in meV (right ordinate). Purple dashed lines represent the sign-flipped negative part of $\Sigma'(\omega) - \mu$. The abscissae are on a symmetric-log scale, with a narrow region (gray shade) on a linear scale that interfaces the sides of different signs. In panels (a), (c), and (e) [(b) and (d)], the original data of $A_{\text{tot}}^f(\omega)$ [$\Sigma(\omega) - \mu$] are downscaled to the plotted data by multiplying the factors specified next to the curves.

Phase diagram.—We apply the above criteria to identify the phases of the VTHF model, as shown in Fig. 1. We focus on $T = 10^{-6}$ meV , much lower than experimentally accessible temperatures. When EPC is off, we find hard-gap phases at $|\nu| = 1, 1.9, 2.9$, except that the TIVC case at $|\nu| = 1$ has a pseudogap. They feature large f -electron contributions to the entropy per MUC, $S^f = \ln 4$ at $|\nu| = 1, 2.9$ and $S^f = \ln 6$ at $|\nu| = 1.9$, which reflect the four- and six-fold degeneracies of the $\text{SU}(4)$ Hubbard term for one (or three, equivalently) and two particles, respectively. The HG phases at $|\nu| = 1.9, 2.9$ are characterized by a gap of $\Delta''(\omega)$ at $\omega = 0$ [Fig. 2(a)]. The HG+OSM phase for VP and KIVC at $|\nu| = 1$ exhibits a Σ pole at $\omega \simeq -1$ meV induced by the Hubbard interaction, on top of the HG [Fig. 2(b)]. A similar Σ pole makes the TIVC case at $|\nu| = 1$ an OSM phase.

Turning on EPC strongly modifies the system at $1.9 \lesssim |\nu| \lesssim 2.5$, where $|\nu^f|$ stays close to 2 due to the strong Hubbard repulsion [16, 61]. For the VP and TIVC orders, S^f vanishes since the spin anti-Hund coupling in H_{EPC} with $J_S \gg J_L$ favors the singlet state $(l, s) = (0, 0)$ of two f electrons (holes) for $\nu^f = 2$ (-2), which is similar to a crystalline-electric-field (CEF) singlet [94]. Here l and s are the quantum numbers associated with the $\text{U}(1)_{\text{orbital}}$ and $\text{SU}(2)_{\text{spin}}$ symmetries, respectively. On the other

hand, for the KIVC order, the orbital-angular-momentum Hund coupling in H_{EPC} with $J_S \ll J_L$ favors the orbital doublet $(l, s) = (\pm 2, 0)$, resulting in $S^f = \ln 2$.

Importantly, the OSM phase at $2 \leq |\nu| \leq \nu_{\text{cr}}$ ($\nu_{\text{cr}} = 2.4, 2.2, 2.5$ for VP, KIVC, and TIVC, respectively) is consistent with experimental observations of robust pseudogap in the AA-stacking region at a similar range of ν [40, 41]. Without EPC and further symmetry breaking (beyond that imposed by the downfolding), the system at $2 \leq |\nu| \leq 2.5$ features f - and c -electron spectral functions peaking around $\omega = 0$ [cf. Fig. 2(c)] [17]. Meanwhile, EPC introduces a Σ pole near $\omega = 0$ that opens a gap in the spectral function [Fig. 2(d)]. The gap formation can be explained by the atomic charge gap increased by H_{EPC} [80], reminiscent of the Janus effect in Hund metals [73–77]: In t_{2g} and e_g systems at half filling, the Hund coupling increases the atomic gap and decreases the critical interaction strength of the Mott transition, favoring an insulating phase; away from half filling, the same coupling decreases the atomic gap, favoring metallicity. We emphasize that the valley-orbital ordering is also crucial, as it shifts “half” filling from $\nu^f = 0$ for the original THF model to $|\nu^f| = 2$ for the VTHF model.

By contrast, the phases at $|\nu| \simeq 1, 3$ are overall less affected by EPC, while the gap disappears in the KIVC case

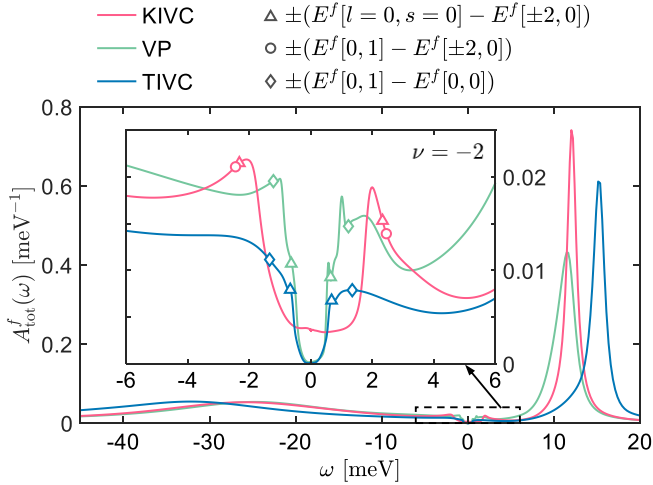


FIG. 3. Local f -electron spectral function at $\nu = -2$ for different orders with EPC, which corresponds to the local density of states in the AA-stacking region. The inset zooms into the low-frequency region, $|\omega| < 6$ meV, which shows pseudogaps. Markers indicate the differences between the lowest-lying energy eigenvalues E^f of the local f -electron Hamiltonian. l and s are orbital and spin quantum numbers, respectively.

at $|\nu| = 2.9$ and the OSM' phases arise in the TIVC case at $|\nu| = 1.9, 3$. Despite the absence of Σ poles, the OSM' phase is strongly correlated; for example, $\Sigma(0)$ clearly deviates from the Hartree value $\Sigma(\pm\infty)$ in Fig. 2(e).

The gapless phase (white regions in Fig. 1) is peculiar since $|S^f|$ is small but nonzero. By analyzing the energy flow diagram and the scaling of $\Sigma''(\omega)$, we identify them as incoherent metals, not Fermi liquids. $S^f > 0$ implies that f electrons are not fully screened since the Fermi-liquid coherence scale is exponentially low ($\lesssim T = 10^{-6}$ meV) due to the small hybridization strength $|\Delta''(0)|$ originating from the small density of states of the Dirac bands near the Fermi level. Such small $|\Delta''|$ is also the reason for the absence of a Kondo insulator phase in our phase diagram. On the other hand, $S^f < 0$ comes from the strong ω -dependence of Δ'' [95–99]. See Ref. [79] for details.

Pseudogap and pairing susceptibilities.—The f -electron pseudogap with side peaks at its edges appears throughout the OSM phase at $2 \leq |\nu| \leq \nu_{\text{cr}}$; see Fig. 3 for the case of $\nu = -2$. The positions of the side peaks align well with spin, orbital, or spin-orbital excitation energy scales [79], which are also given by the splitting of the two-hole (cf. $\nu, \nu^f < 0$) eigenvalues of the local f -electron Hamiltonian, according to the effective Hund couplings in H_{EPC} . In the VP and TIVC cases, the two-hole ground state is the singlet $(l, s) = (0, 0)$. The other two-hole eigenstates are the orbital doublet $(\pm 2, 0)$ and the spin triplet $(0, 1)$. Thus the energy differences $E^f[l = \pm 2, s = 0] - E^f[0, 0]$ and $E^f[0, 1] - E^f[0, 0]$ mean, respectively, the local orbital and spin excitation energies, around which

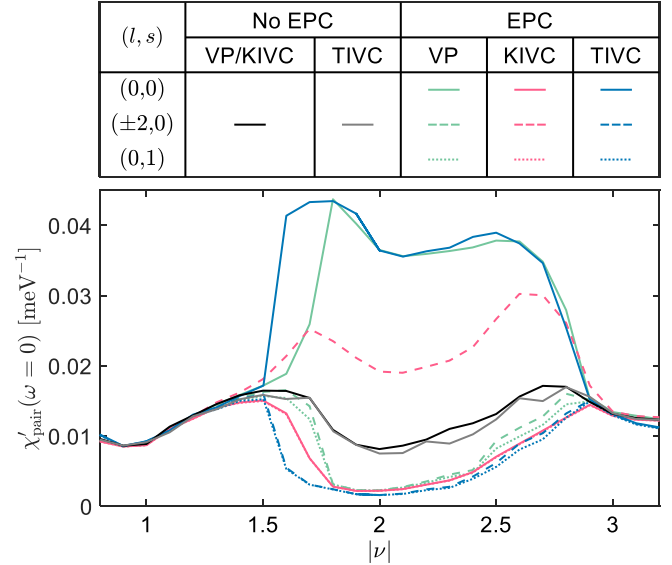


FIG. 4. Static pairing susceptibilities for f -electron pairs with different symmetries, denoted by the quantum numbers (l, s) of the pair creation operators. When EPC is off, the curves for different (l, s) are identical due to the SU(4) symmetry. Solid and dotted magenta lines lie on top of each other.

the side peaks are located. A similar argument holds for the KIVC case, where $(\pm 2, 0)$ is the ground-state doublet, while $(0, 0)$ and $(0, 1)$ are excited states.

Figure 4 displays the static pairing susceptibilities $\chi'_{\text{pair}}(\omega = 0)$ for different symmetries (l, s) of an f -electron pair. For $\nu > 0$, we compute $\chi'_{\text{pair}}(0)$ as the real part of $\chi_{\text{pair}}(\omega) = -i \int_0^\infty dt e^{i(\omega + i0^+)t} \langle [P_{ls}(t), P_{ls}^\dagger(0)] \rangle$ in the active space, where P_{ls}^\dagger creates two f electrons such that $P_{ls}^\dagger|\text{CNP}\rangle$ has quantum numbers (l, s) , and $|\text{CNP}\rangle$ is the vacuum of the active space. Notably, EPC enhances $\chi'_{\text{pair}}(0)$ at $1.6 \lesssim \nu \lesssim 2.8$ for a specific (l, s) component for each valley-ordering, such that the action of P_{ls}^\dagger to the local two- f -electron ground state leads to full f orbitals. Here $l = 0$ (± 2) pair creation implies s -(d -)wave pairing [80]. The case for $\nu < 0$ is similar, after particle-hole transformation.

Discussion.—The OSM phase near $|\nu| = 2$ and the pseudogap with the side peaks, both induced by EPC, constitute the central result of this work. It is another evidence of Hundness—strong correlations arising from (effective) Hund interactions—that the side peaks are associated with spin, orbital, or spin-orbital fluctuations, evocative of orbital resonance features in the spectral function of Hund metals [77, 100–102]. Since those fluctuations are charge-neutral, the side peaks cannot be captured by Hartree-Fock (HF) solutions such as the TIVC \times QSH (quantum spin Hall) order [27–29].

Among the three valley-orbital orders, we conclude that the TIVC result is most consistent with experimental observations at $|\nu| \simeq 2$. $S^f = 0$ means that excess

electrons (or holes) do not form moments and the underlying TIVC order is exposed in the whole system. This result reconciles the STM imaging of TIVC order [41] and the spin-singlet Mott-like feature [32]. Also, the width of the f -electron pseudogap is consistent with the STM measurements on the AA-stacking region [40].

On the other hand, we find large spin-valley-orbital moments corresponding to $S^f = \ln 4$ for general scenarios at $|\nu| \simeq 1, 3$, except for the KIVC case with EPC at $|\nu| \simeq 3$. Given that the f -electron dispersion is very flat, the RKKY interactions between these moments will be ferromagnetic, which can explain the observed symmetry-breaking states at $|\nu| = 1, 3$ in experiments [38, 103, 104].

The range of $1.6 \lesssim \nu \lesssim 2.8$ for enhanced pairing susceptibilities is consistent with the superconducting domes [39–41, 44–46]. These pairs are local, so they may be a precursor to molecular pairing [26], among various proposals of pairing glue [20–23, 105–108]. However, we cannot decisively fix the pairing symmetry of MATBG from our result since valley-orbital fluctuations, which we ignored by choosing the static order, may be important to stabilize pairing. It will be worthwhile to obtain the solutions with broken $U(1)_{\text{charge}}$ symmetry, considering a breakdown of valley-orbital ordering and the role of strain, which is left to future studies.

We thank Andreas Gleis, Minsoo Kim, Fabian Kugler, Jong Yeon Lee, Mathias Pelz, Yi-Jie Wang, and Jan von Delft for fruitful discussions. This work was supported by Samsung Electronics Co., Ltd. (No. IO220817-02066-01), the Global-LAMP Program of the National Research Foundation of Korea (NRF) grant funded by the Ministry of Education (No. RS-2023-00301976), the NRF grants funded by the Korean government (MSIT) (No. RS-2023-00214464, No. RS-2023-00258359, No. RS-2023-NR119931, No. RS-2024-00442710), and the NRF grant funded by the Korean government (MEST) (No. 2019R1A6A1A10073437). Z.-D.S. and G.-D.Z. were supported by National Natural Science Foundation of China (General Program No. 12274005), National Key Research and Development Program of China (No. 2021YFA1401903), and Innovation Program for Quantum Science and Technology (No. 2021ZD0302403).

* These authors contributed equally to this work.

† songzd@pku.edu.cn

‡ sslee@snu.ac.kr

- [1] R. Bistritzer and A. H. MacDonald, Moiré bands in twisted double-layer graphene, *Proc. Natl. Acad. Sci.* **108**, 12233 (2011).
- [2] L. Zou, H. C. Po, A. Vishwanath, and T. Senthil, Band structure of twisted bilayer graphene: Emergent symmetries, commensurate approximants, and Wannier obstructions, *Phys. Rev. B* **98**, 085435 (2018).
- [3] J. Ahn, S. Park, and B.-J. Yang, Failure of Nielsen-

- Ninomiya theorem and fragile topology in two-dimensional systems with space-time inversion symmetry: Application to twisted bilayer graphene at magic angle, *Phys. Rev. X* **9**, 021013 (2019).
- [4] H. C. Po, L. Zou, T. Senthil, and A. Vishwanath, Faithful tight-binding models and fragile topology of magic-angle bilayer graphene, *Phys. Rev. B* **99**, 195455 (2019).
- [5] Z. Song, Z. Wang, W. Shi, G. Li, C. Fang, and B. A. Bernevig, All magic angles in twisted bilayer graphene are topological, *Phys. Rev. Lett.* **123**, 036401 (2019).
- [6] J. Liu, J. Liu, and X. Dai, Pseudo Landau level representation of twisted bilayer graphene: Band topology and implications on the correlated insulating phase, *Phys. Rev. B* **99**, 155415 (2019).
- [7] Z.-D. Song, B. Lian, N. Regnault, and B. A. Bernevig, Twisted bilayer graphene. II. stable symmetry anomaly, *Phys. Rev. B* **103**, 205412 (2021).
- [8] T. Huang, L. Zhang, and T. Ma, Antiferromagnetically ordered Mott insulator and d+id superconductivity in twisted bilayer graphene: a quantum Monte Carlo study, *Sci. Bull.* **64**, 310 (2019).
- [9] T. Soejima, D. E. Parker, N. Bultinck, J. Hauschild, and M. P. Zaletel, Efficient simulation of moiré materials using the density matrix renormalization group, *Phys. Rev. B* **102**, 205111 (2020).
- [10] B.-B. Chen, Y. D. Liao, Z. Chen, O. Vafek, J. Kang, W. Li, and Z. Y. Meng, Realization of topological Mott insulator in a twisted bilayer graphene lattice model, *Nat. Commun.* **12**, 5480 (2021).
- [11] Y. Da Liao, J. Kang, C. N. Breið, X. Y. Xu, H.-Q. Wu, B. M. Andersen, R. M. Fernandes, and Z. Y. Meng, Correlation-induced insulating topological phases at charge neutrality in twisted bilayer graphene, *Phys. Rev. X* **11**, 011014 (2021).
- [12] D. E. Parker, T. Soejima, J. Hauschild, M. P. Zaletel, and N. Bultinck, Strain-induced quantum phase transitions in magic-angle graphene, *Phys. Rev. Lett.* **127**, 027601 (2021).
- [13] J. S. Hofmann, E. Khalaf, A. Vishwanath, E. Berg, and J. Y. Lee, Fermionic Monte Carlo study of a realistic model of twisted bilayer graphene, *Phys. Rev. X* **12**, 011061 (2022).
- [14] T. Wang, D. E. Parker, T. Soejima, J. Hauschild, S. Anand, N. Bultinck, and M. P. Zaletel, Ground-state order in magic-angle graphene at filling $\nu = -3$: A full-scale density matrix renormalization group study, *Phys. Rev. B* **108**, 235128 (2023).
- [15] H. Hu, G. Rai, L. Crippa, J. Herzog-Arbeitman, D. Călugăru, T. Wehling, G. Sangiovanni, R. Valentí, A. M. Tsvelik, and B. A. Bernevig, Symmetric Kondo lattice states in doped strained twisted bilayer graphene, *Phys. Rev. Lett.* **131**, 166501 (2023).
- [16] G. Rai, L. Crippa, D. Călugăru, H. Hu, F. Paoletti, L. de' Medici, A. Georges, B. A. Bernevig, R. Valentí, G. Sangiovanni, and T. Wehling, Dynamical correlations and order in magic-angle twisted bilayer graphene, *Phys. Rev. X* **14**, 031045 (2024).
- [17] G.-D. Zhou, Y.-J. Wang, N. Tong, and Z.-D. Song, Kondo phase in twisted bilayer graphene, *Phys. Rev. B* **109**, 045419 (2024).
- [18] A. Datta, M. J. Calderón, A. Camjayi, and E. Bascones, Heavy quasiparticles and cascades without symmetry breaking in twisted bilayer graphene, *Nat. Commun.* **14**, 5036 (2023).

- [19] Z.-Y. Xiao and S. Zhang, Correlation effects in magic-angle twisted bilayer graphene: An auxiliary-field quantum Monte Carlo study, [arXiv:2405.17808](#).
- [20] F. Wu, A. H. MacDonald, and I. Martin, Theory of phonon-mediated superconductivity in twisted bilayer graphene, *Phys. Rev. Lett.* **121**, 257001 (2018).
- [21] B. Lian, Z. Wang, and B. A. Bernevig, Twisted bilayer graphene: A phonon-driven superconductor, *Phys. Rev. Lett.* **122**, 257002 (2019).
- [22] A. Blason and M. Fabrizio, Local Kekulé distortion turns twisted bilayer graphene into topological Mott insulators and superconductors, *Phys. Rev. B* **106**, 235112 (2022).
- [23] C.-X. Liu, Y. Chen, A. Yazdani, and B. A. Bernevig, Electron- K -phonon interaction in twisted bilayer graphene, *Phys. Rev. B* **110**, 045133 (2024).
- [24] J. F. Dodaro, S. A. Kivelson, Y. Schattner, X. Q. Sun, and C. Wang, Phases of a phenomenological model of twisted bilayer graphene, *Phys. Rev. B* **98**, 075154 (2018).
- [25] M. Angeli, E. Tosatti, and M. Fabrizio, Valley Jahn-Teller effect in twisted bilayer graphene, *Phys. Rev. X* **9**, 041010 (2019).
- [26] Y.-J. Wang, G.-D. Zhou, S.-Y. Peng, B. Lian, and Z.-D. Song, Molecular pairing in twisted bilayer graphene superconductivity, *Phys. Rev. Lett.* **133**, 146001 (2024).
- [27] H. Shi, W. Miao, and X. Dai, Moiré optical phonons dancing with heavy electrons in magic-angle twisted bilayer graphene, [arXiv:2402.11824](#).
- [28] Y.-J. Wang, G.-D. Zhou, B. Lian, and Z.-D. Song, Electron phonon coupling in the topological heavy fermion model of twisted bilayer graphene, [arXiv:2407.11116](#).
- [29] Y. H. Kwan, G. Wagner, N. Bultinck, S. H. Simon, E. Berg, and S. A. Parameswaran, Electron-phonon coupling and competing Kekulé orders in twisted bilayer graphene, [arXiv:2303.13602](#).
- [30] M. Angeli and M. Fabrizio, Jahn-Teller coupling to moiré phonons in the continuum model formalism for small-angle twisted bilayer graphene, *Eur. Phys. J. Plus* **135**, 630 (2020).
- [31] C. Chen, K. P. Nuckolls, S. Ding, W. Miao, D. Wong, M. Oh, R. L. Lee, S. He, C. Peng, D. Pei, Y. Li, S. Zhang, J. Liu, Z. Liu, C. Jozwiak, A. Bostwick, E. Rotenberg, C. Li, X. Han, D. Pan, X. Dai, C. Liu, B. A. Bernevig, Y. Wang, A. Yazdani, and Y. Chen, Strong inter-valley electron-phonon coupling in magic-angle twisted bilayer graphene, [arXiv:2303.14903](#).
- [32] Y. Cao, V. Fatemi, A. Demir, S. Fang, S. L. Tomarken, J. Y. Luo, J. D. Sanchez-Yamagishi, K. Watanabe, T. Taniguchi, E. Kaxiras, R. C. Ashoori, and P. Jarillo-Herrero, Correlated insulator behaviour at half-filling in magic-angle graphene superlattices, *Nature* **556**, 80 (2018).
- [33] Y. Xie, B. Lian, B. Jäck, X. Liu, C.-L. Chiu, K. Watanabe, T. Taniguchi, B. A. Bernevig, and A. Yazdani, Spectroscopic signatures of many-body correlations in magic-angle twisted bilayer graphene, *Nature* **572**, 101 (2019).
- [34] Y. Choi, J. Kemmer, Y. Peng, A. Thomson, H. Arora, R. Polski, Y. Zhang, H. Ren, J. Alicea, G. Refael, F. von Oppen, K. Watanabe, T. Taniguchi, and S. Nadj-Perge, Electronic correlations in twisted bilayer graphene near the magic angle, *Nat. Phys.* **15**, 1174 (2019).
- [35] X. Liu, Z. Wang, K. Watanabe, T. Taniguchi, O. Vafek, and J. I. A. Li, Tuning electron correlation in magic-angle twisted bilayer graphene using Coulomb screening, *Science* **371**, 1261 (2021).
- [36] Y. Saito, J. Ge, K. Watanabe, T. Taniguchi, and A. F. Young, Independent superconductors and correlated insulators in twisted bilayer graphene, *Nat. Phys.* **16**, 926 (2020).
- [37] P. Stepanov, I. Das, X. Lu, A. Fahimniya, K. Watanabe, T. Taniguchi, F. H. L. Koppens, J. Lischner, L. Levitov, and D. K. Efetov, Untying the insulating and superconducting orders in magic-angle graphene, *Nature* **583**, 375 (2020).
- [38] X. Lu, P. Stepanov, W. Yang, M. Xie, M. A. Aamir, I. Das, C. Urgell, K. Watanabe, T. Taniguchi, G. Zhang, A. Bachtold, A. H. MacDonald, and D. K. Efetov, Superconductors, orbital magnets and correlated states in magic-angle bilayer graphene, *Nature* **574**, 653 (2019).
- [39] Y. Cao, D. Chowdhury, D. Rodan-Legrain, O. Rubies-Bigorda, K. Watanabe, T. Taniguchi, T. Senthil, and P. Jarillo-Herrero, Strange metal in magic-angle graphene with near Planckian dissipation, *Phys. Rev. Lett.* **124**, 076801 (2020).
- [40] M. Oh, K. P. Nuckolls, D. Wong, R. L. Lee, X. Liu, K. Watanabe, T. Taniguchi, and A. Yazdani, Evidence for unconventional superconductivity in twisted bilayer graphene, *Nature* **600**, 240 (2021).
- [41] K. P. Nuckolls, R. L. Lee, M. Oh, D. Wong, T. Soejima, J. P. Hong, D. Călugăru, J. Herzog-Arbeitman, B. A. Bernevig, K. Watanabe, T. Taniguchi, N. Regnault, M. P. Zaletel, and A. Yazdani, Quantum textures of the many-body wavefunctions in magic-angle graphene, *Nature* **620**, 525 (2023).
- [42] Y. Choi, H. Kim, C. Lewandowski, Y. Peng, A. Thomson, R. Polski, Y. Zhang, K. Watanabe, T. Taniguchi, J. Alicea, and S. Nadj-Perge, Interaction-driven band flattening and correlated phases in twisted bilayer graphene, *Nat. Phys.* **17**, 1375 (2021).
- [43] A. Kerelsky, L. J. McGilly, D. M. Kennes, L. Xian, M. Yankowitz, S. Chen, K. Watanabe, T. Taniguchi, J. Hone, C. Dean, A. Rubio, and A. N. Pasupathy, Maximized electron interactions at the magic angle in twisted bilayer graphene, *Nature* **572**, 95 (2019).
- [44] Y. Cao, D. Rodan-Legrain, J. M. Park, N. F. Q. Yuan, K. Watanabe, T. Taniguchi, R. M. Fernandes, L. Fu, and P. Jarillo-Herrero, Nematicity and competing orders in superconducting magic-angle graphene, *Science* **372**, 264 (2021).
- [45] Y. Cao, V. Fatemi, S. Fang, K. Watanabe, T. Taniguchi, E. Kaxiras, and P. Jarillo-Herrero, Unconventional superconductivity in magic-angle graphene superlattices, *Nature* **556**, 43 (2018).
- [46] M. Tanaka, J. I.-j. Wang, T. H. Dinh, D. Rodan-Legrain, S. Zaman, M. Hays, B. Kannan, A. Almanakly, D. K. Kim, B. M. Niedzielski, K. Serniak, M. E. Schwartz, K. Watanabe, T. Taniguchi, J. A. Grover, T. P. Orlando, S. Gustavsson, P. Jarillo-Herrero, and W. D. Oliver, Superfluid stiffness and flat-band superconductivity in magic-angle graphene probed by cQED, [arXiv:2406.13740](#).
- [47] H. C. Po, L. Zou, A. Vishwanath, and T. Senthil, Origin of Mott insulating behavior and superconductivity in twisted bilayer graphene, *Phys. Rev. X* **8**, 031089 (2018).
- [48] J. Kang and O. Vafek, Strong coupling phases of partially filled twisted bilayer graphene narrow bands, *Phys. Rev. Lett.* **122**, 246401 (2019).

- [49] M. Xie and A. H. MacDonald, Nature of the correlated insulator states in twisted bilayer graphene, *Phys. Rev. Lett.* **124**, 097601 (2020).
- [50] Y. Zhang, K. Jiang, Z. Wang, and F. Zhang, Correlated insulating phases of twisted bilayer graphene at commensurate filling fractions: A Hartree-Fock study, *Phys. Rev. B* **102**, 035136 (2020).
- [51] N. Bultinck, E. Khalaf, S. Liu, S. Chatterjee, A. Vishwanath, and M. P. Zaletel, Ground state and hidden symmetry of magic-angle graphene at even integer filling, *Phys. Rev. X* **10**, 031034 (2020).
- [52] J. Liu and X. Dai, Theories for the correlated insulating states and quantum anomalous Hall effect phenomena in twisted bilayer graphene, *Phys. Rev. B* **103**, 035427 (2021).
- [53] B. Lian, Z.-D. Song, N. Regnault, D. K. Efetov, A. Yazdani, and B. A. Bernevig, Twisted bilayer graphene. IV. exact insulator ground states and phase diagram, *Phys. Rev. B* **103**, 205414 (2021).
- [54] Z.-D. Song and B. A. Bernevig, Magic-angle twisted bilayer graphene as a topological heavy fermion problem, *Phys. Rev. Lett.* **129**, 047601 (2022).
- [55] H. Shi and X. Dai, Heavy-fermion representation for twisted bilayer graphene systems, *Phys. Rev. B* **106**, 245129 (2022).
- [56] J. Herzog-Arbeitman, J. Yu, D. Călugăru, H. Hu, N. Regnault, O. Vafek, J. Kang, and B. A. Bernevig, Heavy fermions as an efficient representation of atomistic strain and relaxation in twisted bilayer graphene, [arXiv:2405.13880](https://arxiv.org/abs/2405.13880).
- [57] K. Singh, A. Chew, J. Herzog-Arbeitman, B. A. Bernevig, and O. Vafek, Topological heavy fermions in magnetic field, *Nat. Commun.* **15**, 5257 (2024).
- [58] L. L. H. Lau and P. Coleman, Topological mixed valence model for twisted bilayer graphene, [arXiv:2303.02670](https://arxiv.org/abs/2303.02670).
- [59] Y.-Z. Chou and S. Das Sarma, Scaling theory of intrinsic Kondo and Hund's rule interactions in magic-angle twisted bilayer graphene, *Phys. Rev. B* **108**, 125106 (2023).
- [60] Y.-Z. Chou and S. Das Sarma, Kondo lattice model in magic-angle twisted bilayer graphene, *Phys. Rev. Lett.* **131**, 026501 (2023).
- [61] H. Hu, B. A. Bernevig, and A. M. Tsvelik, Kondo lattice model of magic-angle twisted-bilayer graphene: Hund's rule, local-moment fluctuations, and low-energy effective theory, *Phys. Rev. Lett.* **131**, 026502 (2023).
- [62] R. L. Merino, D. Calugaru, H. Hu, J. Diez-Merida, A. Diez-Carlon, T. Taniguchi, K. Watanabe, P. Seifert, B. A. Bernevig, and D. K. Efetov, Evidence of heavy fermion physics in the thermoelectric transport of magic angle twisted bilayer graphene, [arXiv:2402.11749](https://arxiv.org/abs/2402.11749).
- [63] D. Călugăru, H. Hu, R. L. Merino, N. Regnault, D. K. Efetov, and B. A. Bernevig, The thermoelectric effect and its natural heavy fermion explanation in twisted bilayer and trilayer graphene, [arXiv:2402.14057](https://arxiv.org/abs/2402.14057).
- [64] Q. Hu, S. Liang, X. Li, H. Shi, X. Dai, and Y. Xu, Link between cascade transitions and correlated Chern insulators in magic-angle twisted bilayer graphene, [arXiv:2406.08734](https://arxiv.org/abs/2406.08734).
- [65] A. Georges, G. Kotliar, W. Krauth, and M. J. Rozenberg, Dynamical mean-field theory of strongly correlated fermion systems and the limit of infinite dimensions, *Rev. Mod. Phys.* **68**, 13 (1996).
- [66] K. G. Wilson, The renormalization group: Critical phenomena and the Kondo problem, *Rev. Mod. Phys.* **47**, 773 (1975).
- [67] R. Bulla, T. A. Costi, and T. Pruschke, Numerical renormalization group method for quantum impurity systems, *Rev. Mod. Phys.* **80**, 395 (2008).
- [68] A. Weichselbaum and J. von Delft, Sum-rule conserving spectral functions from the numerical renormalization group, *Phys. Rev. Lett.* **99**, 076402 (2007).
- [69] A. Weichselbaum, Tensor networks and the numerical renormalization group, *Phys. Rev. B* **86**, 245124 (2012).
- [70] S.-S. B. Lee and A. Weichselbaum, Adaptive broadening to improve spectral resolution in the numerical renormalization group, *Phys. Rev. B* **94**, 235127 (2016).
- [71] S.-S. B. Lee, J. von Delft, and A. Weichselbaum, Doublon-holon origin of the subpeaks at the Hubbard band edges, *Phys. Rev. Lett.* **119**, 236402 (2017).
- [72] F. B. Kugler, Improved estimator for numerical renormalization group calculations of the self-energy, *Phys. Rev. B* **105**, 245132 (2022).
- [73] P. Werner, E. Gull, and A. J. Millis, Metal-insulator phase diagram and orbital selectivity in three-orbital models with rotationally invariant Hund coupling, *Phys. Rev. B* **79**, 115119 (2009).
- [74] L. de' Medici, Hund's coupling and its key role in tuning multiorbital correlations, *Phys. Rev. B* **83**, 205112 (2011).
- [75] L. de' Medici, J. Mravlje, and A. Georges, Janus-faced influence of Hund's rule coupling in strongly correlated materials, *Phys. Rev. Lett.* **107**, 256401 (2011).
- [76] A. Georges, L. de' Medici, and J. Mravlje, Strong correlations from Hund's coupling, *Annu. Rev. Condens. Ma. P.* **4**, 137 (2013).
- [77] K. M. Stadler, G. Kotliar, A. Weichselbaum, and J. von Delft, Hundness versus Mottness in a three-band Hubbard-Hund model: On the origin of strong correlations in Hund metals, *Ann. Phys.* **405**, 365 (2019).
- [78] B. A. Bernevig, B. Lian, A. Cowsik, F. Xie, N. Regnault, and Z.-D. Song, Twisted bilayer graphene. V. exact analytic many-body excitations in Coulomb hamiltonians: Charge gap, Goldstone modes, and absence of Cooper pairing, *Phys. Rev. B* **103**, 205415 (2021).
- [79] S. Youn, B. Goh, G.-D. Zhou, Z.-D. Song, and S.-S. B. Lee, in preparation.
- [80] See End Matter for additional information on the VTHF Hamiltonian, the effective Hund couplings induced by EPC, DMFT+NRG, atomic charge gap, and pairing symmetries.
- [81] M. Capone, M. Fabrizio, and E. Tosatti, Direct transition between a singlet Mott insulator and a superconductor, *Phys. Rev. Lett.* **86**, 5361 (2001).
- [82] M. Capone, M. Fabrizio, C. Castellani, and E. Tosatti, Strongly correlated superconductivity, *Science* **296**, 2364 (2002).
- [83] M. Capone, M. Fabrizio, C. Castellani, and E. Tosatti, Strongly correlated superconductivity and pseudogap phase near a multiband Mott insulator, *Phys. Rev. Lett.* **93**, 047001 (2004).
- [84] M. Capone, M. Fabrizio, C. Castellani, and E. Tosatti, Colloquium: Modeling the unconventional superconducting properties of expanded A_3C_{60} fullerenes, *Rev. Mod. Phys.* **81**, 943 (2009).
- [85] Y. Nomura, S. Sakai, M. Capone, and R. Arita, Unified understanding of superconductivity and Mott transition in alkali-doped fullerenes from first principles, *Sci. Adv.*

- [1, e1500568 \(2015\)](#).
- [86] B. A. Bernevig, Z.-D. Song, N. Regnault, and B. Lian, Twisted bilayer graphene. III. interacting Hamiltonian and exact symmetries, *Phys. Rev. B* **103**, 205413 (2021).
- [87] T. A. Costi, A. C. Hewson, and V. Zlatic, Transport coefficients of the Anderson model via the numerical renormalization group, *J. Phys. Condens. Matter* **6**, 2519 (1994).
- [88] P. Sun and G. Kotliar, Understanding the heavy fermion phenomenology from a microscopic model, *Phys. Rev. Lett.* **95**, 016402 (2005).
- [89] D. Tanasković, K. Haule, G. Kotliar, and V. Dobrosavljević, Phase diagram, energy scales, and nonlocal correlations in the Anderson lattice model, *Phys. Rev. B* **84**, 115105 (2011).
- [90] L. De Leo, M. Civelli, and G. Kotliar, $t = 0$ heavy-fermion quantum critical point as an orbital-selective Mott transition, *Phys. Rev. Lett.* **101**, 256404 (2008).
- [91] L. De Leo, M. Civelli, and G. Kotliar, Cellular dynamical mean-field theory of the periodic Anderson model, *Phys. Rev. B* **77**, 075107 (2008).
- [92] A. Gleis, S.-S. B. Lee, G. Kotliar, and J. von Delft, Emergent properties of the periodic Anderson model: A high-resolution, real-frequency study of heavy-fermion quantum criticality, *Phys. Rev. X* **14**, 041036 (2024).
- [93] T. Pruschke, R. Bulla, and M. Jarrell, Low-energy scale of the periodic Anderson model, *Phys. Rev. B* **61**, 12799 (2000).
- [94] S. Yotsuhashi, K. Miyake, and H. Kusunose, Non-Fermi liquid behavior of u-impurity with f₂-singlet ground state, *J. Phys. Soc. Japan* **71**, 389 (2002).
- [95] A. K. Zhuravlev, Negative impurity magnetic susceptibility and heat capacity in a Kondo model with narrow peaks in the local density of electron states, *Phys. Met. Metallogr.* **108**, 107 (2009).
- [96] A. K. Zhuravlev and V. Y. Irkhin, Kondo effect in the presence of van Hove singularities: A numerical renormalization group study, *Phys. Rev. B* **84**, 245111 (2011).
- [97] D. Mastrogiuseppe, A. Wong, K. Ingersent, S. E. Ulloa, and N. Sandler, Kondo effect in graphene with Rashba spin-orbit coupling, *Phys. Rev. B* **90**, 035426 (2014).
- [98] A.-K. Wu, D. Bauernfeind, X. Cao, S. Gopalakrishnan, K. Ingersent, and J. H. Pixley, Aubry-André Anderson model: Magnetic impurities coupled to a fractal spectrum, *Phys. Rev. B* **106**, 165123 (2022).
- [99] A. S. Shankar, D. O. Oriekhov, A. K. Mitchell, and L. Fritz, Kondo effect in twisted bilayer graphene, *Phys. Rev. B* **107**, 245102 (2023).
- [100] K. M. Stadler, Z. P. Yin, J. von Delft, G. Kotliar, and A. Weichselbaum, Dynamical mean-field theory plus numerical renormalization-group study of spin-orbital separation in a three-band hund metal, *Phys. Rev. Lett.* **115**, 136401 (2015).
- [101] F. B. Kugler, S.-S. B. Lee, A. Weichselbaum, G. Kotliar, and J. von Delft, Orbital differentiation in hund metals, *Phys. Rev. B* **100**, 115159 (2019).
- [102] F. B. Kugler, M. Zingl, H. U. R. Strand, S.-S. B. Lee, J. von Delft, and A. Georges, Strongly correlated materials from a numerical renormalization group perspective: How the fermi-liquid state of sr₂ruo₄ emerges, *Phys. Rev. Lett.* **124**, 016401 (2020).
- [103] S. Grover, M. Bocarsly, A. Uri, P. Stepanov, G. Di Battista, I. Roy, J. Xiao, A. Y. Meltzer, Y. Myasoedov, K. Pareek, K. Watanabe, T. Taniguchi, B. Yan, A. Stern, E. Berg, D. K. Efetov, and E. Zeldov, Chern mosaic and Berry-curvature magnetism in magic-angle graphene, *Nat. Phys.* **18**, 885 (2022).
- [104] P. Stepanov, M. Xie, T. Taniguchi, K. Watanabe, X. Lu, A. H. MacDonald, B. A. Bernevig, and D. K. Efetov, Competing zero-field Chern insulators in superconducting twisted bilayer graphene, *Phys. Rev. Lett.* **127**, 197701 (2021).
- [105] J. Yu, Y.-A. Chen, and S. Das Sarma, Euler-obstructed Cooper pairing: Nodal superconductivity and hinge Majorana zero modes, *Phys. Rev. B* **105**, 104515 (2022).
- [106] E. Khalaf, S. Chatterjee, N. Bultinck, M. P. Zaletel, and A. Vishwanath, Charged skyrmions and topological origin of superconductivity in magic-angle graphene, *Sci. Adv.* **7**, eabf5299 (2021).
- [107] M. Christos, S. Sachdev, and M. S. Scheurer, Nodal band-off-diagonal superconductivity in twisted graphene superlattices, *Nat. Commun.* **14**, 7134 (2023).
- [108] S. F. Islam, A. Y. Zyuzin, and A. A. Zyuzin, Unconventional superconductivity with preformed pairs in twisted bilayer graphene, *Phys. Rev. B* **107**, L060503 (2023).
- [109] D. M. Basko and I. L. Aleiner, Interplay of Coulomb and electron-phonon interactions in graphene, *Phys. Rev. B* **77**, 041409 (2008).
- [110] T. O. Wehling, E. Şaşıoğlu, C. Friedrich, A. I. Lichtenstein, M. I. Katsnelson, and S. Blügel, Strength of effective Coulomb interactions in graphene and graphite, *Phys. Rev. Lett.* **106**, 236805 (2011).
- [111] M. Schüler, M. Rösner, T. O. Wehling, A. I. Lichtenstein, and M. I. Katsnelson, Optimal Hubbard models for materials with nonlocal Coulomb interactions: Graphene, silicene, and benzene, *Phys. Rev. Lett.* **111**, 036601 (2013).
- [112] R. Žitko and T. Pruschke, Energy resolution and discretization artifacts in the numerical renormalization group, *Phys. Rev. B* **79**, 085106 (2009).
- [113] A. Weichselbaum, Non-abelian symmetries in tensor networks: A quantum symmetry space approach, *Ann. Phys. (N.Y.)* **327**, 2972 (2012).
- [114] A. Weichselbaum, X-symbols for non-Abelian symmetries in tensor networks, *Phys. Rev. Res.* **2**, 023385 (2020).
- [115] A. Weichselbaum, QSpace - an open-source tensor library for Abelian and non-Abelian symmetries, *SciPost Phys. Codebases* , 40 (2024).

END MATTER

Details of H_{VTHF} .—We explain the derivation of H_{VTHF} first for the VP case. The f electrons in the VP state at CNP have the same valley, say $-$ without loss of generality. Then the active, excess f electrons at $\nu > 0$ are all from the $+$ valley, $(f_{\mathbf{R},+1,\sigma}, f_{\mathbf{R},-1,\sigma}) = (f_{\mathbf{R},1,+,\sigma}^{\text{THF}}, f_{\mathbf{R},2,+,\sigma}^{\text{THF}})$, where $f_{\mathbf{R}l\sigma}$ and $f_{\mathbf{R}\alpha\eta\sigma}^{\text{THF}}$ annihilate, respectively, an active f electron from the VTHF model and an f electron from the unprojected THF model. ($\alpha = 1, 2$, $\eta = \pm$, $l = \pm 1$, $\sigma = \uparrow, \downarrow$) Projecting the non-interacting part of the THF model Hamiltonian in the flat band limit [17, 54] onto the active space, we get

$$h^c(\mathbf{k}) = \begin{pmatrix} 0_{2 \times 2} & v_*(k_x\sigma_0 + ik_y\sigma_z) \\ v_*(k_x\sigma_0 - ik_y\sigma_z) & 0_{2 \times 2} \end{pmatrix}, \quad (4)$$

$$h^{cf}(\mathbf{k}) = e^{-\lambda^2|\mathbf{k}|^2} [\gamma\sigma_0 + v'_*(k_x\sigma_x + k_y\sigma_y), 0_{2 \times 2}]^\dagger,$$

whose rows and columns are indexed by $a = 1, 2, 3, 4$, except for the columns of $h^{cf}(\mathbf{k})$ indexed by $l = +1, -1$. $\sigma_{0,x,y,z}$ are the Pauli matrices. We adopt the parameters from Ref. [54]: $v_* = -4303 \text{ meV}\cdot\text{\AA}$, $\lambda = 0.414/\sin(\frac{\theta_m}{2})\text{\AA}$ with magic angle $\theta_m = 1.05^\circ$, $\gamma = -24.75 \text{ meV}$, and $v'_* = 1622 \text{ meV}\cdot\text{\AA}$. The interacting part of H_{VTHF} is obtained by projecting that of the THF

model onto the active space, after treating the inactive f and c electrons as a static background. The resulting interactions are the SU(4) Hubbard U_1 interaction and H_{nonloc} , comprising the c - c density-density (V), c - f density-density ($W_{a=1,2,3,4}$), and c - f exchange (J) interactions. (We neglect the nearest-neighbor f - f interaction (U_2) [16].)

The KIVC (TIVC) state, which has the order parameter $(\sigma_y\tau_y)$ ($(\sigma_x\tau_x)$), is obtained by applying a flat (chiral) U(4) rotation [54] to the VP state. Here $\sigma_{0,x,y,z}$ and $\tau_{0,x,y,z}$ are the Pauli matrices for orbital (α) and valley (η), respectively. We choose $f_{\mathbf{R},\pm 1,\sigma} = \frac{1}{\sqrt{2}}(f_{\mathbf{R},1,\pm,\sigma}^{\text{THF}} \mp f_{\mathbf{R},2,\mp,\sigma}^{\text{THF}})$ for KIVC and $f_{\mathbf{R},\pm 1,\sigma} = \frac{1}{\sqrt{2}}(f_{\mathbf{R},1,\pm,\sigma}^{\text{THF}} + f_{\mathbf{R},2,\mp,\sigma}^{\text{THF}})$ for TIVC [54, 79]. The resulting H_{VTHF} for the KIVC or TIVC case has h^c , h^{cf} , Hubbard U_1 , and H_{nonloc} identical to those for the VP case, except that the TIVC takes $v'_* = 0$ [79].

Details of H_{EPC} .—The effective local f -electron interaction arises in the full THF model, by integrating out all (Γ and K , acoustic and optical) phonon degrees of freedom [28]. Projecting the interaction term [cf. Eqs. (72)–(76) of Ref. [28]] onto the active space [28, 79], we get

$$H_{\text{EPC}} = \frac{1}{2} \sum_{\mathbf{R}\sigma\sigma'} \begin{pmatrix} -J'_a & 0 & 0 & 0 \\ 0 & J'_c & -J'_b & 0 \\ 0 & -J'_b & J'_c & 0 \\ 0 & 0 & 0 & -J'_a \end{pmatrix}_{m'l', ml} f_{\mathbf{R}l'\sigma}^\dagger f_{\mathbf{R}m'\sigma'}^\dagger f_{\mathbf{R}m\sigma'} f_{\mathbf{R}l\sigma} \quad (5)$$

$$= \sum_{\mathbf{R}} \left[-J'_a \sum_{l=\pm 1} \frac{N_{\mathbf{R}l}^f (N_{\mathbf{R}l}^f - 1)}{2} + J'_b \left(\frac{N_{\mathbf{R},1}^f N_{\mathbf{R},-1}^f}{2} + 2\mathbf{S}_{\mathbf{R},1} \cdot \mathbf{S}_{\mathbf{R},-1} \right) + J'_c N_{\mathbf{R},1}^f N_{\mathbf{R},-1}^f \right],$$

where the rows and columns of the 4×4 matrix in the first line are indexed by $(m^{(l)}, l^{(l)}) = (1, 1), (1, -1), (-1, 1), (-1, -1)$, and $N_{\mathbf{R}l}^f = \sum_{\sigma} f_{\mathbf{R}l\sigma}^\dagger f_{\mathbf{R}l\sigma}$. The strengths of $J'_{a,b,c}$ depend on the valley-orbital order,

$$(J'_a, J'_b, J'_c) = \begin{cases} (\frac{1}{2}J_a + K, & J_b + K, & \frac{1}{2}J_a), & \text{(VP)}, \\ (\frac{\lambda_{\text{RG}}}{2}J_d + K, & \frac{\lambda_{\text{RG}}}{2}J_e + \frac{3}{2}K, & \frac{\lambda_{\text{RG}}}{2}J_d), & \text{(KIVC)}, \\ (\frac{\lambda_{\text{RG}}}{2}J_d + K, & J_b + \frac{\lambda_{\text{RG}}}{2}J_e + \frac{5}{2}K, & -\frac{\lambda_{\text{RG}}}{2}J_d - K), & \text{(TIVC)}, \end{cases} \quad (6)$$

where $(J_a, J_b, J_d, J_e) = (0.96, 1.60, 1.30, 1.19) \text{ meV}$ and $\lambda_{\text{RG}} \in [1, 3.2]$ is the renormalization effect from electrons and K -phonon states [28, 109]. $K = -0.11 \times 10^{-3}U_0$ depends on the on-site Hubbard repulsion $U_0 \in [3, 9] \text{ eV}$ of carbon atom [110, 111] [cf. Eqs. (84)–(87) of Ref. [28]]. We use $\lambda_{\text{RG}} = 2.6$ and $U_0 = 9 \text{ eV}$ in our calculation. Rephrasing Eq. (5), we get $J_S = J'_b$, $J_L = \frac{1}{4}J'_a + \frac{1}{8}J'_b + \frac{1}{4}J'_c$, and $\tilde{U} = -\frac{1}{2}J'_a + \frac{1}{4}J'_b + \frac{1}{2}J'_c$ for Eq. (2) in the main text.

DMFT details.—Our DMFT self-consistency loop is nested, having outer and inner loops. The outer loop involves the \mathbf{k} -space integration of correlators and the NRG

impurity solver step. After applying Hartree mean-field decoupling to H_{nonloc} , our effective impurity model has two active f orbitals as impurity and the corresponding two bath channels. After the NRG obtains $\Sigma(\omega)$, we run the inner, charge self-consistency loop, where μ is determined so that ν^f and ν^c are self-consistent in consideration of the Hartree mean-fields and satisfy $\nu = \nu^f + \nu^c$, for a given target ν .

In the THF and VTHF models, the f orbitals form a lattice, but the c bands form a continuum. That is, the \mathbf{k} -space of the c bands is unbounded. When we

evaluate $G^f(\mathbf{k} \in 1\text{MBZ}, \omega)$ in the outer loop, we include the contribution from $[G^c(\mathbf{k} + \mathbf{G}, \omega)]^{-1}$ for $\mathbf{G} = 0$ (1MBZ) and also \mathbf{G} 's pointing to six reciprocal primitive cells adjacent to the 1MBZ, which is necessary to capture the full ω dependence of the hybridization function $\Delta(\omega)$. If only $\mathbf{G} = 0$ is considered, then the high-frequency part of $\Delta(\omega)$ gets truncated, which leads to artifacts in the Kondo temperature, filling, etc.

NRG details.—We use the logarithmic discretization parameter $\Lambda = 4$ and perform z averaging over $n_z = 2$ discretization grids [112]. We exploit $U(1)_{\text{charge}} \times SU(4)_{\text{spin,orbital}}$ [$U(1)_{\text{charge}} \times U(1)_{\text{orbital}} \times SU(2)_{\text{spin}}$] symmetry when EPC is off (on), by using the QSpace tensor library [113–115]. In iterative diagonalization, up to $N_{\text{keep}} = 3,500$ (5,000) symmetry multiplets are kept when EPC is off (on). Discrete spectral data of correlation functions are obtained using the full-density-matrix NRG [68, 69] and then adaptively broadened [70]. We use the symmetric improved estimator of the self-energy [72] that greatly ameliorates the accuracy for given N_{keep} .

Atomic charge gap.—Table I lists the eigenstates and eigenvalues of the local f -electron interactions (Hubbard U_1 and H_{EPC}). The atomic charge gap at integer filling ν^f is given by $\Delta_{\text{at}} = E_{\text{min}}^f[n^f = \nu^f + 1] + E_{\text{min}}^f[n^f = \nu^f - 1] - 2E_{\text{min}}^f[n^f = \nu^f]$, where $E_{\text{min}}^f[n^f]$ means the lowest energy for a given n^f . Hence we get

$$\Delta_{\text{at}}|_{n^f=1,3} = \begin{cases} U_1 - \frac{3}{2}J_S + 2J_L + \tilde{U}, & (\text{VP, TIVC}), \\ U_1 - 2J_L + \tilde{U}, & (\text{KIVC}), \end{cases} \quad (7)$$

$$\Delta_{\text{at}}|_{n^f=2} = \begin{cases} U_1 + 3J_S - 2J_L + \tilde{U}, & (\text{VP, TIVC}), \\ U_1 + 6J_L + \tilde{U}, & (\text{KIVC}). \end{cases}$$

We see $\Delta_{\text{at}}|_{n^f=1,3} < U_1$ and $\Delta_{\text{at}}|_{n^f=2} > U_1$, a manifestation of the Janus effect of Hundness.

Pairing symmetries.—We discuss the pairing symmetries associated with the favored pairing fluctuations

by EPC in different orders. The unprojected original THF model preserves D_6 point group, whose generators $g \in \{C_{3z}, C_{2z}, C_{2x}\}$ are represented in the unprojected ($f_{\alpha\eta\sigma}^{\text{THF}}$) basis (here we omit index \mathbf{R} for brevity) as $C_{3z} = e^{i\frac{2\pi}{3}\sigma_z\tau_z}$, $C_{2z} = \sigma_x\tau_x$, $C_{2x} = \sigma_x\tau_0$.

The TIVC order with order parameter $\langle\sigma_x\tau_x\rangle$ preserves the D_6 point group, with the symmetry operators on the projected ($f_{l\sigma}$) basis given by $C_{3z} = e^{i\frac{2\pi}{3}\tilde{\sigma}_z}$, $C_{2z} = \tilde{\sigma}_0$, and $C_{2x} = \tilde{\sigma}_x$. Here, $\tilde{\sigma}_{0,x,y,z}$ are the Pauli matrices for the valley-orbital (l) of the active f electrons. The EPC-favored (l, s) = (0, 0) pairing forms the A_1 representation, which equals (up to a normalization factor) to the projected s -wave pairing of the unprojected model [26]. While the d -wave state is the local two-particle ground state in the unprojected model under the chosen parameters (Fig. 6 of Ref. [28]), the projection omits off-diagonal components between the active and inactive bases and makes the s -wave state the ground state. From Fig. 4, we observe that pairing susceptibility is enhanced for channels associated with the local two-particle ground state. Therefore, incorporating the inactive basis or considering valley-orbital fluctuations may change the favored pairing channel.

The KIVC order with order parameter $\langle\sigma_y\tau_y\rangle$ breaks the C_{2x} symmetry but preserves a projective D_6 (dubbed as D_6') group generated by $C_{3z} = e^{i\frac{2\pi}{3}\tilde{\sigma}_z}$, $C_{2z} = -\tilde{\sigma}_z$, and $C_{2x}' = \tilde{\sigma}_x$, where C_{2x}' represents C_{2x} followed by a valley π -rotation τ_z . The EPC-favored ($\pm 2, 0$) pairings form the E_2 representations of D_6' , corresponding (up to a normalization factor) to the projected d -wave E_2 pairing of the unprojected model.

This analysis can also be applied to the VP state, which breaks the C_{2z} symmetry while respecting a projective D_6 group. In this case, the EPC-favored (0, 0) pairing is obtained by projecting the valley-polarized A_1 s -wave pairing of the unprojected model [79].

n^f	l	s	Degeneracy	f -electron eigenstates	E^f
0	0	0	1	$ \text{CNP}\rangle$	0
1	± 1	$\frac{1}{2}$	4	$\{f_{1\uparrow}^\dagger, f_{1\downarrow}^\dagger, f_{-1\uparrow}^\dagger, f_{-1\downarrow}^\dagger\} \text{CNP}\rangle$	0
		± 2	0	2	$\{f_{1\uparrow}^\dagger f_{1\downarrow}^\dagger, f_{-1\uparrow}^\dagger f_{-1\downarrow}^\dagger\} \text{CNP}\rangle$
2	0	0	1	$\frac{1}{\sqrt{2}}(f_{1\uparrow}^\dagger f_{-1\downarrow}^\dagger - f_{1\downarrow}^\dagger f_{-1\uparrow}^\dagger) \text{CNP}\rangle$	$U_1 - \frac{3}{2}J_S + 2J_L + \tilde{U}$
		1	3	$\{\frac{1}{\sqrt{2}}(f_{1\uparrow}^\dagger f_{-1\downarrow}^\dagger + f_{1\downarrow}^\dagger f_{-1\uparrow}^\dagger), f_{1\uparrow}^\dagger f_{-1\uparrow}^\dagger, f_{1\downarrow}^\dagger f_{-1\downarrow}^\dagger\} \text{CNP}\rangle$	$U_1 + \frac{1}{2}J_S + 2J_L + \tilde{U}$
3	± 1	$\frac{1}{2}$	4	$\{f_{1\uparrow}^\dagger f_{1\downarrow}^\dagger f_{-1\downarrow}^\dagger, f_{1\uparrow}^\dagger f_{1\downarrow}^\dagger f_{-1\uparrow}^\dagger, f_{1\downarrow}^\dagger f_{-1\uparrow}^\dagger f_{-1\downarrow}^\dagger, f_{1\uparrow}^\dagger f_{-1\uparrow}^\dagger f_{-1\downarrow}^\dagger\} \text{CNP}\rangle$	$3U_1 + 2J_L + 3\tilde{U}$
4	0	0	1	$f_{1\uparrow}^\dagger f_{1\downarrow}^\dagger f_{-1\uparrow}^\dagger f_{-1\downarrow}^\dagger \text{CNP}\rangle$	$6U_1 + 4J_L + 6\tilde{U}$

TABLE I. The atomic energy eigenvalues and eigenstates of active f electrons according to local interactions (Hubbard U_1 and H_{EPC}). n^f is quantum number associated with the $U(1)_{\text{charge}}$ symmetry. We omit the index \mathbf{R} for the brevity. The atomic ground-state energy for the KIVC (VP or TIVC) case with EPC is color-coded in red (blue). |CNP) denotes the inactive f -electron background at CNP.